



A comparison of the high-temperature oxidation behaviour of conventional wrought and laser beam melted Inconel 625

Nicolas Ramenatte^{a,*}, Annabelle Vernouillet^b, Stéphane Mathieu^a, Aurélie Vande Put^b, Michel Vilasi^a, Daniel Monceau^b

^a Institut Jean Lamour, UMR7198, Université de Lorraine - CNRS, 2 allée André Guinier, BP 50840, 54 011, Nancy Cedex, France

^b CIRIMAT, UMR 5085, Université de Toulouse - CNRS, INPT, ENSIACET, 4 allée Emile Monso, BP 44362, 31 030, Toulouse Cedex 4, France

ARTICLE INFO

Keywords:

- A. Nickel
- A. Superalloys
- C. Selective oxidation

ABSTRACT

The microstructure and oxidation resistance of Laser Beam Melted (LBM) and Conventionally Manufactured (CM) Inconel 625 alloys were studied at 900 °C and 1050 °C. The microstructure of the LBM samples was cellular, with Nb and Mo segregations located at the cell walls. At 900 °C, the oxidation rate was similar for both materials but was clearly higher for the LBM material at 1050 °C. This high oxidation rate induced poor oxide scale compactness, void formation in the subsurface region and the formation of a high amount of $\text{Nb}_{1.5}\text{Cr}_{0.5}\text{O}_4$ at the alloy-oxide interface.

1. Introduction

Nickel-chromium alloys are currently used because of their high strength, excellent fabrication properties, and high resistance to high-temperature degradation effects, such as oxidation and carburization [1]. Inconel 625 has many advantages that enable its use in the wide temperature range from cryogenic conditions to 1000 °C. Its strength is derived from the strengthening effect exerted by molybdenum and niobium on its nickel-chromium matrix. Precipitation-hardening treatments can also be performed in order to obtain the required mechanical properties [2]. The alloy is generally manufactured using the conventional metallurgy route, i.e., by casting, hot- or cold-rolling and annealing. However, manufacturing of components with complex geometries requires time-consuming machining operations or welding treatments. These operations can be avoided by using three-dimensional (3D) additive manufacturing that enables complex designs and material cost saving [3]. Various techniques are now available and used in industry to manufacture large technological pieces: electron beam melting (EBM), laser beam melting (LBM), direct metal deposition (DMD) [4,5], and powder bed binder jet-printing (BJP) [6].

More than any other technique, 3D manufacturing produces specific microstructures and surface defects. The relationship between those defects and the employed printing parameters (Laser Power, Laser scan speed, etc.) was investigated by many authors [7–11]. Surface roughness and surface reactivity of the pieces obtained by 3D manufacturing remain some common issues of these techniques, as shown by

Sanviemvongsak et al. [12] for the nickel based alloy Inconel 718. They reported that the oxidation behaviour of this alloy in air at 1000 °C is independent of the 3D printing process (Laser or Electron Beam Melting). Once taken into account the real developed area, the mass gain followed a parabolic-like kinetics in air up to 1000 °C, in agreement with the oxidation behavior of CM materials [13]. Recent studies [14] also showed that the volume density energy (VED) has an impact on the oxidation resistance of Inconel 718 at 850 °C. For a small VED value (70 J.mm^{-3}), the oxidation rate was two orders of magnitude higher than that of a specimen made with a higher VED value (110 J.mm^{-3}).

While many investigations [15–18] have been carried out on the oxidation behaviour of conventional Inconel 625 in air, there has been less work on the high-temperature reactivity of the 3D manufactured Inconel 625 [19].

In the present study, the oxidation behaviour at 900 and 1050 °C in air is reported for Inconel 625 manufactured layer-by-layer using laser beam melting (LBM) and by conventional manufacturing (CM). The microstructure and the chemical composition were analysed in-depth by scanning electron microscopy (SEM) and electron probe micro analysis (EPMA) in order to determine their influence on the oxidation rate and corrosion products.

* Corresponding author.

E-mail address: nicolas.ramenatte@univ-lorraine.fr (N. Ramenatte).

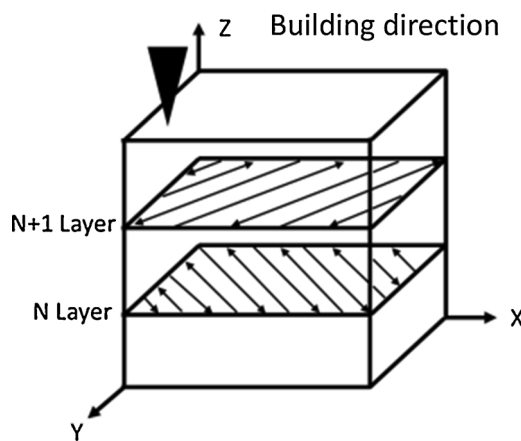


Fig. 1. Schematic description of the 3D building strategy.

2. Materials and methods

2.1. Materials

The pieces were manufactured by Poly-Shape (Salon de Provence in France) with a LBM instrument which was used with a gas-atomized commercial Inconel 625 powder that was supplied by Praxair and had a mean grain diameter of 40 µm. The LBM instrument used a laser fibre with a capacity of 400 W. The laser beam width was in the range of 80–115 µm. For the layer by layer construction (Fig. 1), a backward and forward deposition pattern was employed to deposit in the plane. Then the laser scan direction was altered by 45° to deposit the next layer. Argon served as the shielding gas ($P = 1$ bar) in order to minimize oxidation. The samples were obtained from a 1.5 mm thick plate. To compare the properties of the LBM material with the properties of the CM material, an Inconel 625 sheet was purchased from Goodfellow. The material was supplied in solution annealed condition. The chemical composition of alloys was quantified using electron probe micro-analyses (EPMA) and pure metals as calibration specimens. Results are shown for both Inconel 625 batches (LBM and CM) in Table 1. The measurements have showed that the LBM printing conditions induced a slight composition deviation of minor elements from the composition of the conventional material. In particular, Co, Mn and Si contents were lower than the detection threshold for these analyses (approximately 0.05 % wt.) and were lower in the LBM material than in the CM material.

2.2. Oxidation resistance

For reliable data assessment, the tests were performed in lab air in a furnace at 900 °C and 1050 °C for 400 h and 50 h, respectively, for 5-sample batches of the LBM and CM alloys. The raw as-received surface state and surface after grinding (1200 grit SiC paper) were evaluated for the alloys. The mass gain of the samples was determined by manual weighing using a balance with an accuracy of ± 0.1 mg.

Isothermal oxidation was followed at 900 °C and 1050 °C using a Setsys Evolution 16 SETARAM thermobalance and a symmetric

SETARAM TAG1750 thermobalance with a 0.1 µg sensitivity, respectively. Industrial dry air was introduced in the reaction chamber at 1.5 L.h⁻¹ (gas velocity 7.4 mm.s⁻¹ at 1050 °C). Samples were heated at 20 °C.min⁻¹ up to the test temperature and cooled down at 5 °C.min⁻¹.

2.3. Microstructure observations

For microstructure observations, the samples were mechanically ground on SiC paper and then polished with colloidal silica. Observation of the longitudinal, transverse and horizontal sections of the as-deposited 3D samples was carried out using an OLYMPUS Provis optical microscope and a FEI XL30 scanning electron microscope after chemical etching (mixture of 5 ml H₂O₂ and 95 ml HCl). Cross-sections of the oxide layer were obtained by extracting thin lamellas from the oxidized samples with a dual focused ion beam (FIB) scanning electron microscope system (Helios Nanolab 600i, FEI) using the in situ lift-out technique. A high-resolution transmission electron microscope (JEOL ACCEL ARM 200F-Cold FEG employing a C_s-corrector for the correction of the spherical aberration) was used to perform the microstructure characterization. The chemical analyses were done with an energy dispersive X-ray (EDX) spectrometer (JEOL Centurio EDS 1 sr) coupled to the transmission electron microscope. The crystal structures of the corrosion products were identified by XRD (INEL CPS 590; X-ray beam conditions: 40 kV, 40 mA) using a Co K_α radiation (0.1789 nm).

3. Results

3.1. Initial microstructures characterization

Optical micrographs of the initial microstructures are shown in Fig. 2a for the alloy processed by conventional route. Fig. 2b shows the micrographs for the alloy obtained using the additive manufacturing method. The microstructure of the conventional Inconel 625 (Fig. 2a) consisted of an equiaxed grain structure. FCC austenitic phase (Fm 3 m) with a lattice parameter of 0.359 nm was determined by XRD measurements. The grain size was evaluated from the image analysis to be within 15 µm. Carbonitride (Nb,Ti)(C,N) particles were also homogeneously distributed and their size reached 10–12 µm.

The print strategy for the LBM alloy led, after grinding, to the microstructure presented in Fig. 2b in the X-Y and Z-Y planes. There is no difference between the microstructure in the Z-X and Z-Y planes. The layer-by-layer fabrication stages yielded a microstructure characterized by a succession of Gaussian-shaped marks in the Z-Y and Z-X planes with a curvature in the opposite direction to the laser source. An example of a boundary delimiting the fusion bath (melted pool) is shown in Fig. 3b (Z-Y plane). These boundaries were highlighted after chemical etching because of the micro-segregation that occurred after successive melting passes. For the observations made on the surface perpendicular to the laser beam (Fig. 2b X-Y), the microstructure observations revealed both the laser width and the building strategy. The lattice parameter was evaluated as 0.361 nm by XRD, and the grains were columnar; the grain size was approximately 12 µm in width and several hundred micrometers in length in the building direction.

Higher magnification observations by SEM revealed that this special microstructure consisted of columnar dendrites and small cells (Fig. 3).

Table 1

Current average composition of conventionally manufactured (CM) and laser beam melted (LBM) Inconel 625 specimens determined using EPMA (% wt.) (DT: detection threshold).

Grades	Ni	Cr	Fe	Mo	Nb	Co	Mn	Al	Ti	Si	Closure
CM	61.7 ± 0.1	21.7 ± 0.2	3.8 ± 0.1	8.6 ± 0.3	3.1 ± 0.3	0.13 ± 0.01	0.41 ± 0.01	0.14 ± 0.01	0.20 ± 0.01	0.16 ± 0.01	100.1
LBM	60.0 ± 0.6	22.2 ± 0.2	4.3 ± 0.1	8.9 ± 0.1	3.6 ± 0.2	< DT	0.12 ± 0.01	0.09 ± 0.02	0.19 ± 0.02	< DT ± 0.02	99.4

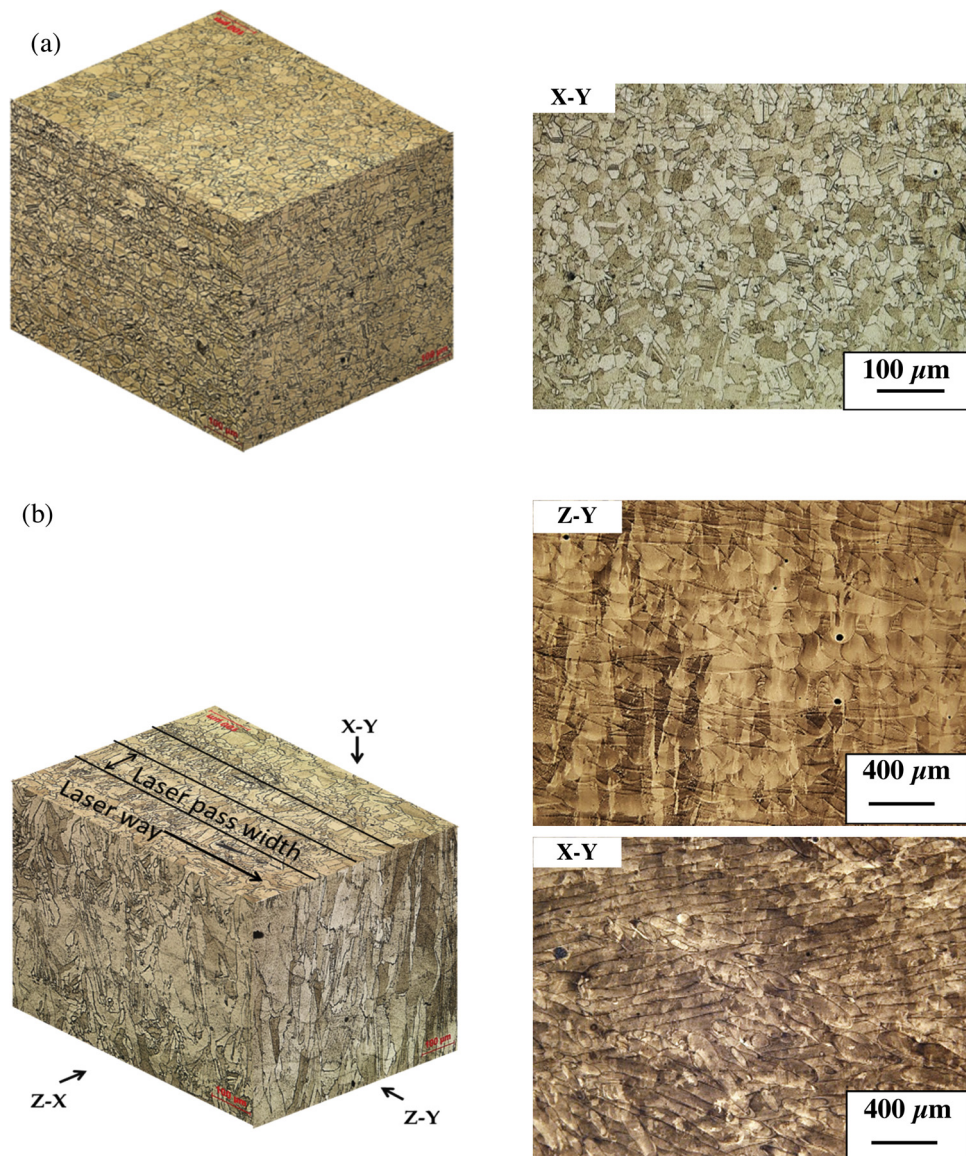


Fig. 2. Cross-sections of Inconel 625 after chemical etching: a) conventional material (b) LBM material.

The dendritic structure extended over several layers, demonstrating the continuity between the successive layers (Fig. 3a). The columnar dendrite direction did not perfectly match the building direction along the Z direction, as shown in Fig. 3b. The orientation deviation arises because the growth of the dendritic structure was closely related to the heat flux direction and to the crystal orientation during the solidification process. In Fig. 3b and c, primary dendrites showing very short secondary dendrite arms are displayed. In some locations, the microstructure was constituted only of small cells (Fig. 3d). These microstructure features are indicative of the very high cooling rate associated to the high laser scan rate employed ($\sim 10 \text{ cm.s}^{-1}$). The microstructure in the X-Y plane was similar to the Z-Y one presented in Fig. 3.

X-ray mappings (Fig. 4) were obtained using a FIB lamella extracted in these peculiar regions. The results showed Nb and Mo segregations that are considered to be responsible of the observed cellular microstructure. By contrast, Cr and Ni atoms were uniformly distributed. TEM EDS chemical composition measurements showed that the cell core contains 5.1 % at. of Nb and 2.1 % at. of Mo whereas the walls contents are 8.0 % at. of Nb and 6.6 % at. of Mo. MC, M₆C carbides or Laves phases were not detected by XRD measurements, STEM-TEM and SEM-EDS analysis.

3.2. Oxidation tests

3.2.1. Furnace exposures in lab air

The oxidation behaviour of the LBM samples was assessed at 900 and 1050 °C in air using the raw as-received printed surface. Mass gains after 400 h and 50 h exposures to 900 and 1050 °C, respectively, for the 5-sample batches are reported in Fig. 5. It was decided to oxidize the samples for 400 h at 900 °C to improve the weight measurement accuracy. After 400 h of oxidation at 900 °C, the mass gains of all samples were quite similar. They ranged from 0.7 to 0.9 mg/cm².

At 1050 °C, the mass gains of raw LBM samples after 50 h varied significantly from 2.1 mg.cm^{-2} to 3.9 mg.cm^{-2} . According to Sanvimevongsak et al. [12], such a behaviour could be due to the high surface roughness associated with the 3D printing method. To support this hypothesis, a confocal microscopy study of the external surface (Fig. 6a) and a SEM cross-section characterization of the outer part of the LBM samples (Fig. 6b and c) were carried out. The as-received printed surfaces had an arithmetic mean height (Sa) of $10 - 12 \mu\text{m}$. Moreover, the microstructure of the subsurface was strongly altered compared to the microstructure of the bulk. First, the outer region consisted mainly of a coarse equiaxed dendritic structure (the border

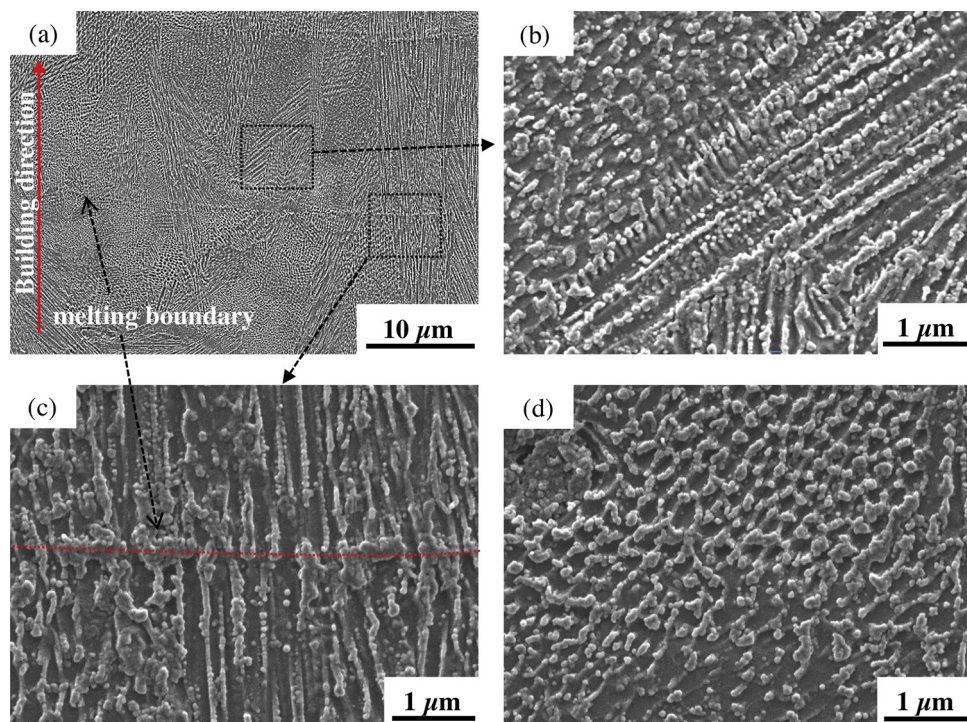


Fig. 3. Microstructure characterization (SEM) of the bulk of LBM Inconel 625 in the Z-Y plan after chemical etching: a) at low magnification, b) at high magnification showing cellular and dendritic structure; c) at the melting boundary (labelled by the dotted line); d) at the location of the cellular structure.

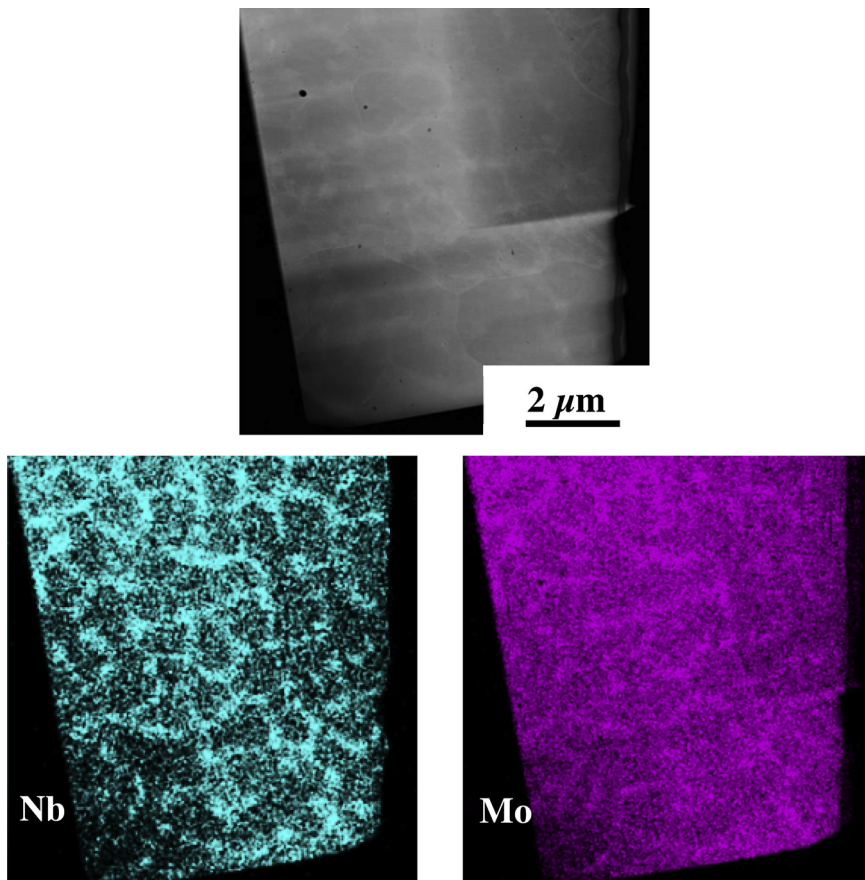


Fig. 4. HAADF-STEM image and relative X-ray maps of the microstructure of the LBM alloy. The results show that $\text{Nb}(\text{L}_\alpha)$ and $\text{Mo}(\text{L}_\alpha)$ segregations are responsible for the cellular microstructure observed in Fig. 3.

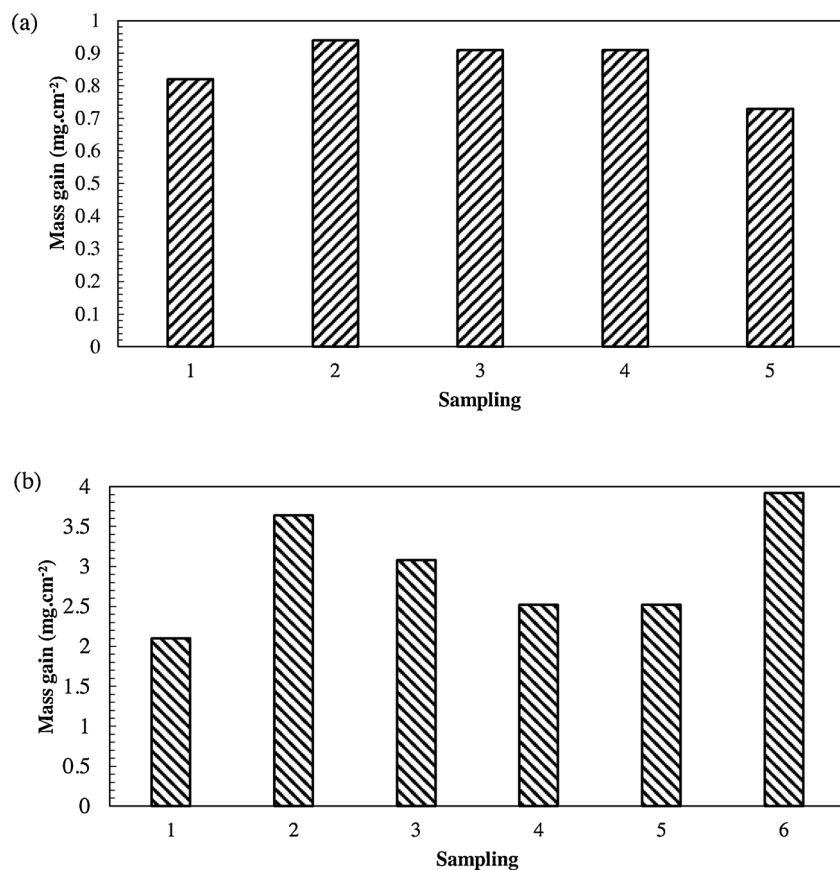


Fig. 5. Mass gains of the as-manufactured LBM-Inconel 625 after isothermal oxidation in still lab air with exposures of a) 400 h at 900 °C and for b) 50 h at 1050 °C.

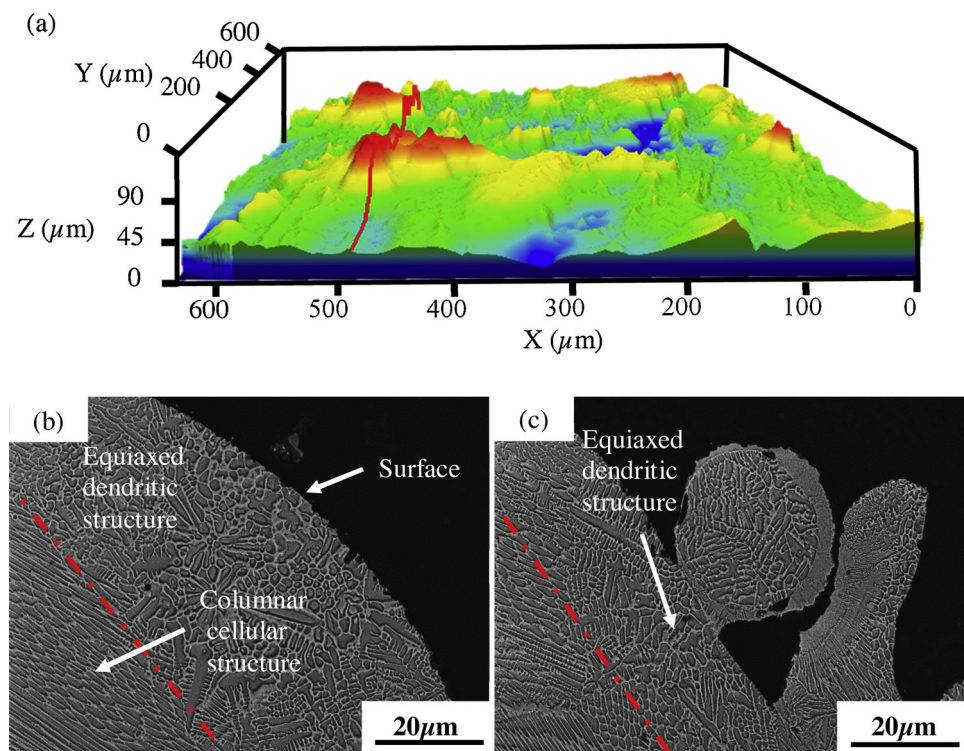


Fig. 6. Surface characterization of the as-manufactured LBM Inconel 625: a) three-dimensional reconstruction of the surface using a confocal microscope; b) and c) SEM cross-sections showing the equiaxed dendritic structure at the surface and the columnar cellular structure underneath.

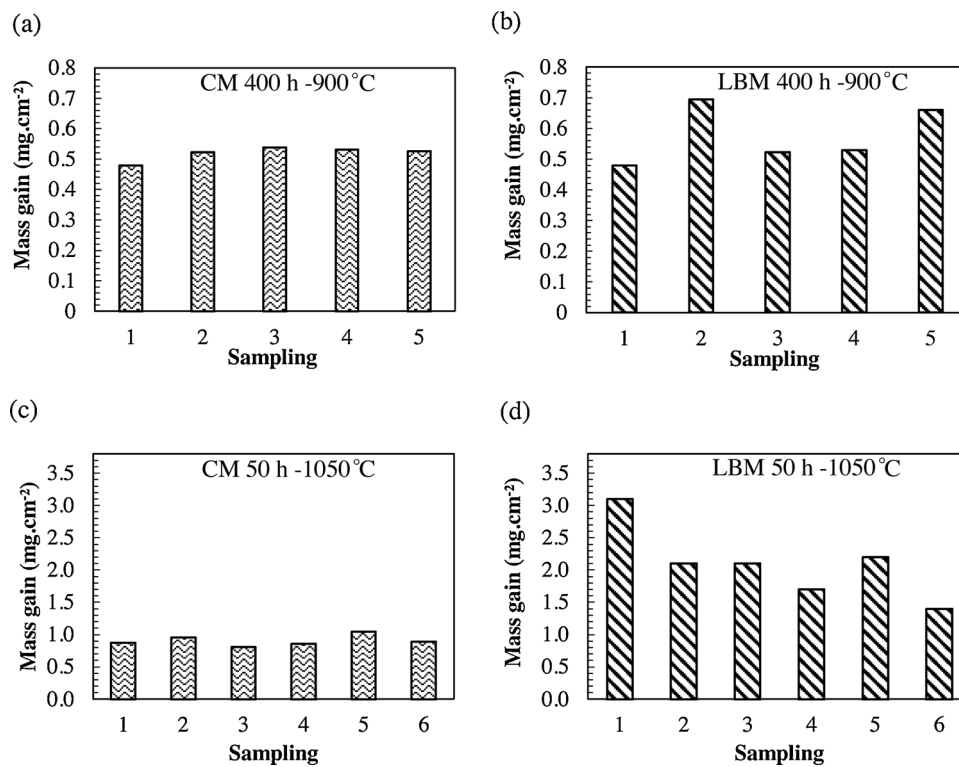


Fig. 7. Mass gains of the ground specimens after isothermal oxidation in still lab air for a duration of 400 h for CM (a), and LBM (b) at 900 °C and for a duration of 50 h for CM (c), and LBM (d) at 1050 °C.

between this region and the bulk one is indicated by a dotted line in Fig. 6). Second, heterogeneous structures developed in this outer region due to the presence of partially melted particles.

Then, all surfaces were automatically ground up to 1200 grit SiC paper with the same time and load (15 N). This treatment should allow the comparison of the oxidation behaviour of the LBM and CM 625 materials.

Fig. 7 presents the mass gains of the ground specimens after 400 h and 50 h exposures at 900 and 1050 °C, respectively, for the LBM and CM batches. The mass gain values reached in average 0.55 mg.cm⁻² after 400 h in air at 900 °C, for both the LBM and CM materials. Two of the LBM 625 samples showed a slightly higher mass gain (0.7 mg.cm⁻²) in comparison to the other LBM tested samples. By contrast, the mass gains at 1050 °C of all ground LBM samples were systematically higher (~2.9 mg.cm⁻² in average) than those of the CM materials (~1 mg.cm⁻²). The values at 1050 °C for the LBM samples also showed large differences, with mass gains varying from 1.5 to 3.1 mg.cm⁻².

3.2.2. Thermogravimetric measurements

Thermogravimetric measurements were performed for 50 h at 900 and 1050 °C on samples with a ground surface (1200 grit SiC paper) to evaluate the isothermal oxidation kinetics of the CM and LBM 625 materials. Fig. 8 shows the mass gain vs time curves at 900 °C (Fig. 8a) and 1050 °C (Fig. 8b) for the CM and LBM ground 625 materials. For improved data reliability, two specimens were tested in each case.

At 900 °C, the results show that the oxidation rates of the samples manufactured by the conventional method and LBM are similar. Overall, the oxidation kinetics follow a parabolic rate law. The complete law [20] was used to deduce the parabolic oxidation constant k_p . The two conventional Inconel 625 samples exhibited rate constants of 4.0×10^{-13} and $3.0 \times 10^{-13} \text{ g}^2.\text{cm}^{-4}.\text{s}^{-1}$, whereas the values for the LBM samples were 4.6×10^{-13} and $5.9 \times 10^{-13} \text{ g}^2.\text{cm}^{-4}.\text{s}^{-1}$.

By contrast, the mass gain vs time curves recorded at 1050 °C showed a larger manufacturing process dependency than at 900 °C (Fig. 7b). Similar to the exposures performed in a furnace with lab air,

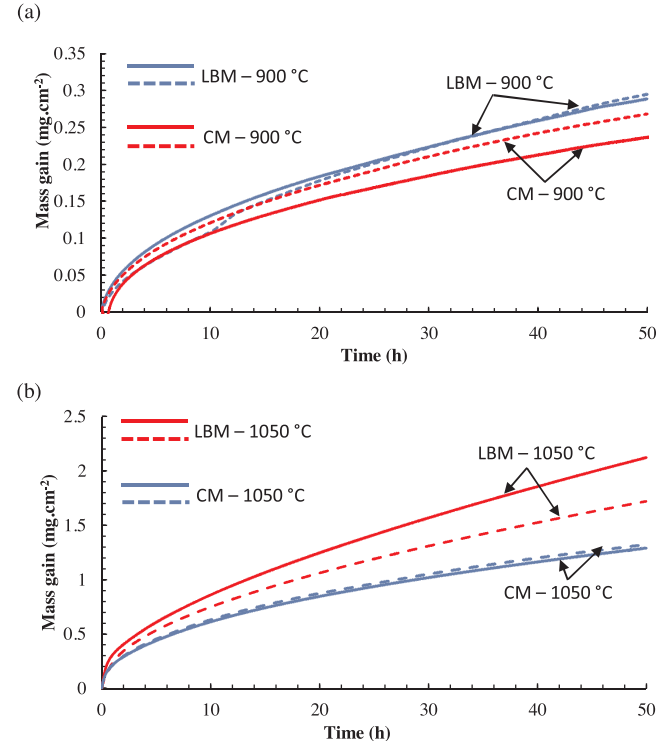


Fig. 8. Mass gains vs time recorded during isothermal oxidation of two ground (P1200) CM specimens (in blue) and two ground LBM-specimens (in red) of Inconel 625: a) at 900 °C and b) at 1050 °C. (For interpretation of the references to colour in this figure legend, the reader is referred to the web version of this article).

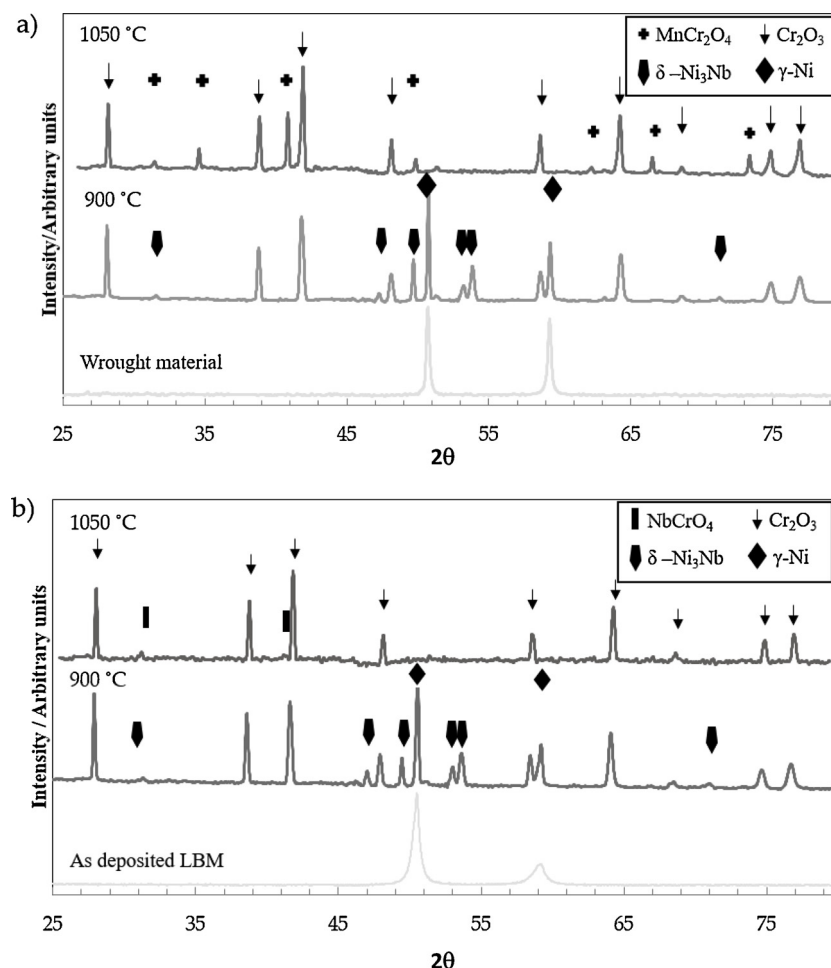


Fig. 9. X-ray diffraction patterns collected at an incidence of 9° for wrought materials and after 400 h and 50 h oxidation at 900 °C and 1050 °C, respectively, in air for a) conventional and b) LBM materials.

CM alloys exhibited very similar mass variation and k_p values (8.0×10^{-12} and $8.3 \times 10^{-12} \text{ g} \cdot \text{cm}^{-4} \cdot \text{s}^{-1}$), whereas differences were observed for the LBM materials, and higher k_p values were determined (1.82×10^{-11} and $3.5 \times 10^{-11} \text{ g} \cdot \text{cm}^{-4} \cdot \text{s}^{-1}$).

3.2.3. Post-oxidation characterization

X-ray diffraction was carried out on the CM and LBM batches after high temperature exposure in air (Fig. 9). The results showed that Cr_2O_3 was mainly formed at 900 and 1050 °C, independently of the manufacturing process. Low intensity X-ray peaks of $(\text{MnCr})_3\text{O}_4$ ($\text{Fd } \bar{3} \text{ m}$) were observed.

After oxidation at 900 °C, the intermetallic compound $\delta\text{-Ni}_3\text{Nb}$ was identified for both alloys. X-ray peaks of this phase may also be present in the diffractogram of the CM samples after oxidation at 1050 °C. The peaks of this compound did not appear for the LBM samples at 1050 °C. In the latter case, the X-ray peaks of rutile structure ($P4_2/\text{mmm}$) with low intensity were identified: these peaks can be associated with either TiO_2 or the interoxidic NbCrO_4 compound that crystallizes with the same crystal structure.

Fig. 10 compares the cross-sections for conventional and LBM Inconel 625 oxidized 50 h in lab air at 900 °C and 1050 °C. At 900 °C (Fig. 10a and b), an oxide scale of approximately 2 μm thickness ($1.6 \pm 0.3 \mu\text{m}$ and $1.5 \pm 0.3 \mu\text{m}$ for CM and LBM respectively) was observed for both alloys. As a result of chromium depletion, the formation of a Nb-rich layer occurred in the subsurface region. XRD confirmed that these precipitates crystallized according to the $\delta\text{-Ni}_3\text{Nb}$. Internal oxidation of aluminium extended over 7–8 μm in the subsurface regions of both alloys. However, the morphology of the internal

oxidation was quite different in the two studied materials. In the CM sample, alumina decorated the alloy grain boundaries, showing that intergranular oxidation developed. For the LBM samples, the amount of internal oxide was much lower than that for the CM alloy.

At 1050 °C (Fig. 10c and d), the oxide scale thicknesses were close to 12 μm. The oxide scale thickness for the LBM sample can be underestimated because the outer part of the oxide scale was very brittle, as shown in Fig. 10d, and was partly broken during metallographic preparation. The oxide scale mainly consisted of chromia topped by a $(\text{MnCr})_3\text{O}_4$ spinel layer of 1 μm thickness in the case of the CM alloy. This top layer was not observed for the LBM alloy. The chromia layer appeared dense in the case of the CM alloy whereas, it was poorly compact for LBM alloy and fall down during handling.

The alloy-oxide region was investigated by STEM-EDX spectroscopy (Fig. 11) on a FIB cross-sectional lamella extracted from an oxidized LBM sample at 1050 °C. The study indicated that the light grey oxide was Mo-, Nb- and Cr-rich for both alloys. The measurements of the chemical composition by EDS in TEM demonstrated that this oxide corresponds to $\text{Nb}_{1.5}\text{Cr}_{0.5}\text{O}_4$. This observation confirmed the XRD data that indicated the presence of a NbCrO_4 oxide with a rutile type crystal structure ($P4_2/\text{mmm}$). It formed a continuous layer in the case of LBM at the alloy-oxide interface, but this was not the case for the CM material. In this region, the presence of cracks was systematically observed for the LBM samples.

Some differences can also be noticed regarding internal oxidation. For the conventional material, internal oxidation extended over 20 μm into the substrate in the form of TiO_2 and Al_2O_3 localized at the grain boundaries (Fig. 9c). For LBM samples, it was difficult to distinguish

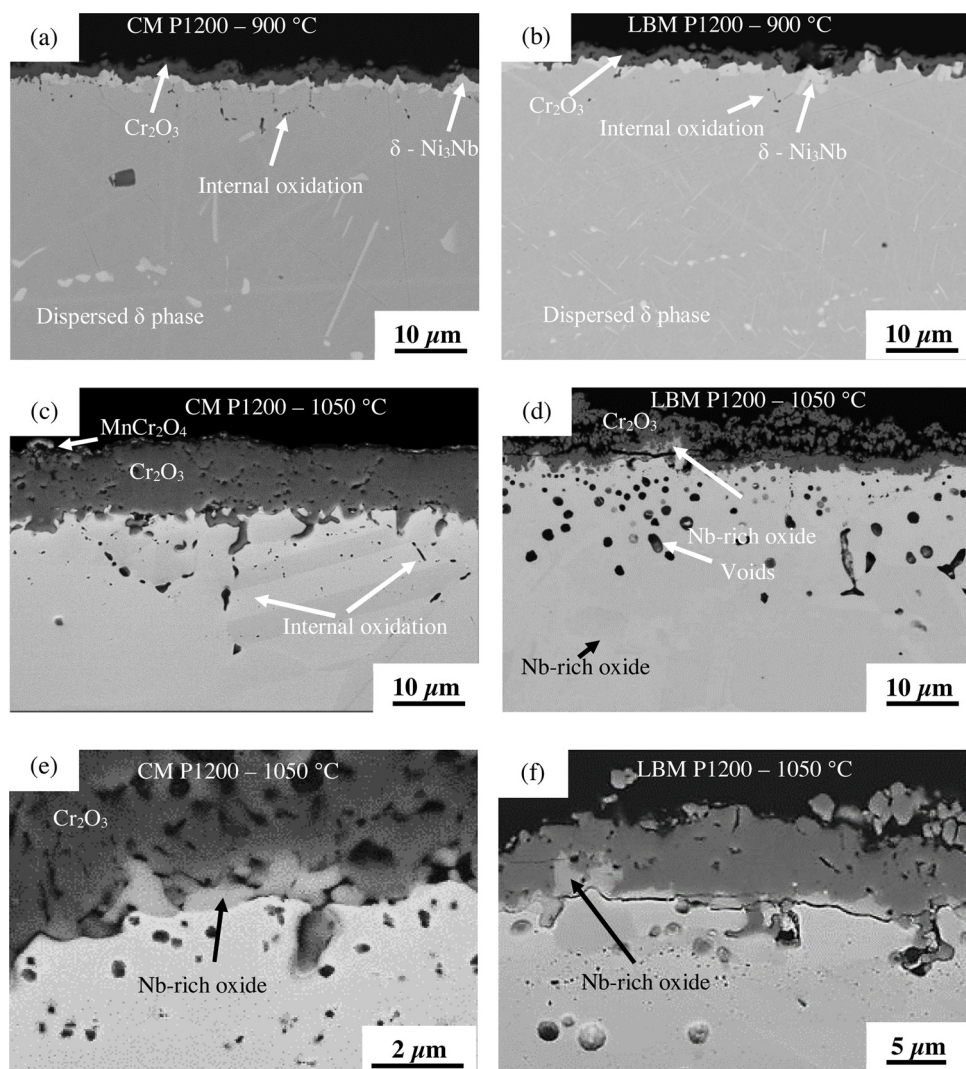


Fig. 10. Post-oxidation cross-sections for the CM and LBM Inconel 625 : a) and b) 400 h in lab air at 900 °C; c) and d) 50 h at 1050 °C ; e) and f) high magnification images of the oxide/substrate interface for c) and d) sections respectively.

internal oxidation from void formation. A high number of voids developed within 20 μm of the subsurface region.

4. Discussion

4.1. Microstructure of LBM made Inconel 625

For the conventionally manufactured alloy (supplied in solution annealed condition) used as reference for the oxidation assessment in the present study, the grain size was approximately 15 μm. XRD measurements showed that the lattice parameter of the LBM samples was slightly higher ($a = 0.361$ nm) than that ($a = 0.359$ nm) obtained for the CM samples. The literature [21] reported that the LBM Inconel 625 structure corresponds to an austenitic matrix supersaturated with Mo and Nb. The absence of precipitates (γ' , Laves phases and carbides) in these alloys results from the high cooling rates ($10^6\text{-}10^7$ °C/s) of the additive manufacturing process [21,23].

Optical microscopy observations of the bulk show the succession of Gaussian-shaped marks, with the curvature in the opposite direction to the laser source. These features are similar to those developed in the welding process, in which generally a "V" shape morphology [7,22] and a textured grain structure in the direction of construction [23] are observed. Therefore, the bulk microstructure of as-manufactured LBM samples consists of columnar grains that are ~12 μm wide and several

hundred micrometers long in the longitudinal direction to the laser beam. Voids that can be present with this technique [24] are not observed in these as-manufactured LBM samples. Higher magnification observations (Fig. 2) of the bulk microstructure showed columnar dendrites and very small cells (0.4–1 μm), similar to those observed by several authors [21,25] for Ni-based superalloys obtained by additive manufacturing. The local cooling rate (c) can be deduced from the distance between the primary dendrite arms (d_{sp}) using Eq. (1):

$$d_{sp} = \alpha c^\beta \quad (1)$$

where α and β are fitting parameters that depend on the nature of the alloy and the cooling temperature. These values were deduced by fitting phase field simulations ($\alpha = 800$ μm and $\beta = -0.57$) [23,25]. The calculated cooling rate with $d_{sp} = 400$ nm was approximately 2.3×10^6 °C/s for the studied LBM samples, which was in full agreement with the literature reports on the LBM process [23]. X-ray mappings (Fig. 3) indicated that the cellular microstructure results from Nb and Mo segregation. Antonsson [26] has mentioned that the cooling rate has a strong effect on Nb segregation because its solubility in the γ phase decreases with the increase of the cooling rate. Moreover, Xiao et al. [27] have shown that the laser mode directly influenced Nb segregation. The performed chemical analyses showed that the cell core contains 5.1 % at. of Nb and 2.1 % at. of Mo whereas the walls contents are 8.0 % at. of Nb and 6.6 % at. of Mo.

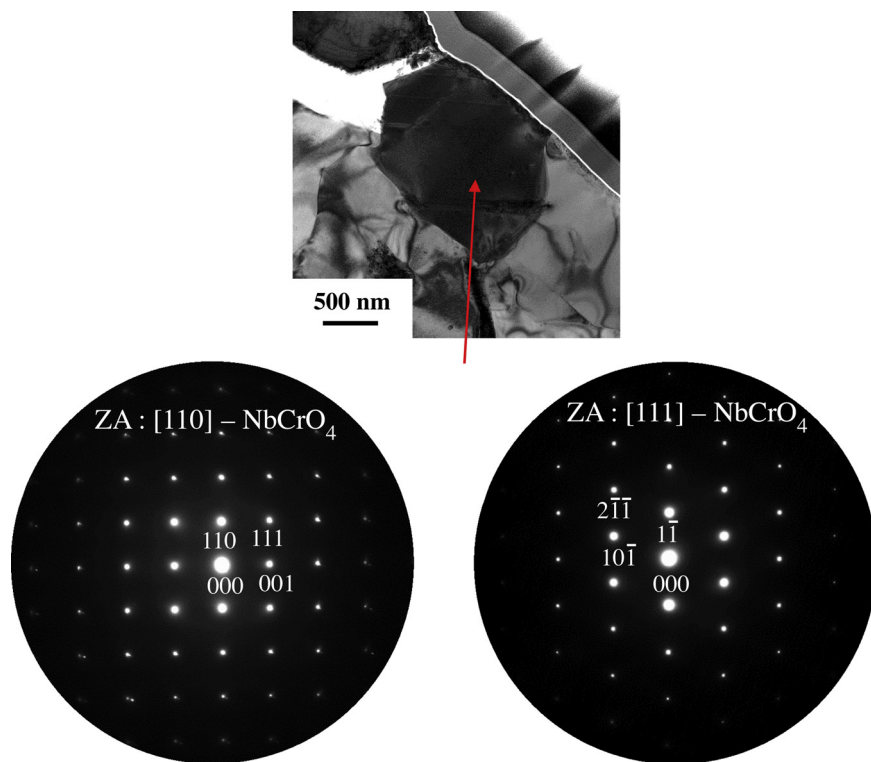


Fig. 11. Bright-field image for Cr and Nb-rich oxide at the metal-oxide region of the oxidized LBM sample after exposure to 1050 °C and electron diffraction patterns along the [110] and [111] zone axes.

Table 2

Solute distribution coefficient (k) calculated both from the present chemical composition measurements and by Hu et al. [21] for the Fe, Cr, Mo and Nb.

Solute distribution coefficient			
Cr	Fe	Mo	Nb
This study	1.04	1.17	0.77
Hu et al. [21]	1.04	1.31	0.77

The calculation of the solute distribution coefficient (k) (Table 2), i.e., the ratio of the atomic fractions in the cell core and walls location was in agreement with the calculation conducted by Hu et al. [21]. With k values that diverged from 1, Mo and especially Nb were prone to segregate in the intercell and interdendritic spaces.

The microstructure of the subsurface region was strongly altered in comparison to the microstructure of the bulk. The outer region mainly consisted of a coarse equiaxed dendritic structure and heterogeneous structures that develop due to the partially melted particles. This result was in accordance with the work by Hu et al. [21], who showed that the temperature decreased from the top to the bottom of the molten pool. Consequently, the solidification rate decreased from the bottom to the top. This configuration promotes the formation of a dendritic structure in the bottom region when the molten pool solidified and the formation of equiaxed grains on top. For the layers in depth (bulk), the equiaxed microstructure was remelted during the next layer deposition and thus finally disappeared. This finding may explain why the equiaxed structure was observed only close to the external surface and why for the as-manufactured LBM alloy, the characterization shows that bulk and as-received surfaces have different microstructures.

4.2. Oxidation behaviour

The oxidation temperatures of 900 °C and 1050 °C were chosen for this study because these temperatures correspond to the operating

temperature and to the maximal temperature of use, respectively. It should be mentioned that at temperatures of 1050 °C and above, the growth rate of the chromium-containing oxide scale can be affected by the sublimation of $\text{Cr}_2\text{O}_3(s)$ into $\text{Cr}_2\text{O}_3(g)$ [18,28]. In the present case, the exposure times were relatively short and the gas flow rates were very low. Therefore the relative rapid scale growth rate is not strongly affected by weight loss as a result of formation of volatile species.

The results of the oxidation tests performed on as-received LBM samples indicate differences between various samples at the test temperature of 1050 °C. This discrepancy can be assigned to the surface state resulting of the manufacturing method. It is now well-known that surface roughness can be high and can affect the area of the reactive surface and, therefore, the oxidation properties. A confocal microscope was used to evaluate the surface roughness of the 6 LBM samples. Their arithmetic mean height (Sa) was 10–12 μm in all cases. Confocal measurements also allow the determination of the developed area for the LBM samples. On average, the developed area was 1.4 times the area from the dimensional sample measurements. Sanviemvongsak et al. [12] also evaluated the developed area from surface topography measurements in order to rationalize the oxidation rates of EBM and LBM Inconel 718. They observed the same ratio and showed that taking this ratio into account led to similar oxidation rates for conventional, EBM and LBM Inconel 718 alloys at 850 °C. Taking into account this value of 1.4 for the present study for the LBM samples, the mass gain per surface area after 400 h varied from 0.54 to 0.68 $\text{mg}\cdot\text{cm}^{-2}$ at 900 °C and from 1.5 to 2.8 $\text{mg}\cdot\text{cm}^{-2}$ at 1050 °C. These values must be compared to 0.5 and 1 $\text{mg}\cdot\text{cm}^{-2}$ (Fig. 7) estimated for the same duration for the ground CM materials at 900 °C and 1050 °C, respectively. The differences in the mass variation between the 3D as received samples and CM specimens can therefore be partially explained by the surface roughness for the 900 °C oxidation tests ($0.5 \text{ mg}\cdot\text{cm}^{-2} \times 1.4 = 0.7 \text{ mg}\cdot\text{cm}^{-2}$). However, the difference between the mass gains at 1050 °C was too high to be explained by surface roughness. Therefore, all surfaces were automatically ground to avoid the influence of the reactive area and the heterogeneous surface state finishing linked to

the manufacturing process itself.

This surface preparation had as a result, that similar mass gains were obtained after 400 h exposure at 900 °C for the CM and LBM alloys. This result was not found for samples exposed at 1050 °C, for which the oxidation rate of the ground LBM samples remained higher than that of the CM materials and showed large discrepancies between various samples.

In addition, the oxidation kinetics were assessed using thermogravimetric experiments. The k_p values at 900 °C were the highest for the LBM materials but remained very close to the values of the CM materials. The k_p values of the CM samples were 3–4 times lower than those determined for the LBM alloys at 1050 °C. The oxidation kinetics of the conventional Inconel 625 evaluated in air over the range of 600–1250 °C were reported [15,16] to obey to a parabolic law because of the chromia growth limitation by solid state transport. However, the present mass gain vs time curves recorded at 1050 °C clearly deviated from the pure parabolic behaviour after 25 h.

These results must also be discussed with respect to subsurface evolutions. Indeed, it was determined both by cross-section observation and X-ray diffraction that chromium consumption as a result of the protective chromia layer growth induced the formation of the $\delta\text{-Ni}_3\text{Nb}$ (Nb and Mo rich) phase at the alloy-oxide interface at 900 °C. For Ni-based superalloys [29] and below 1100 °C, niobium and molybdenum enrichments at this interface were previously reported to be responsible for the formation of a continuous layer of $\delta\text{-Ni}_3(\text{Nb},\text{Mo})$. Chyrkin et al. mentioned the presence of $\delta\text{-Ni}_3(\text{Nb},\text{Mo})$ at 900 and 1000 °C [30]. They demonstrated that a change in the niobium chemical potential accompanied chromium depletion. Consequently, niobium diffused towards the alloy-oxide interface because a niobium chemical potential gradient develops in the Cr-depleted zone.

At 1050 °C, the $\delta\text{-Ni}_3\text{Nb}$ was not observed because of the higher solubility (10 % at. vs 7 % at. at 900 °C) of Nb in the austenitic Ni-rich matrix [31] at this temperature. Nevertheless, niobium enrichment occurred at the alloy-oxide interface in the form of a more or less continuous interoxidic $\text{Nb}_{1.5}\text{Cr}_{0.5}\text{O}_4$ layer for the LBM samples. This oxide was both identified by electron diffraction and EDS analyses in TEM (Fig. 10).

Rolland [17] also mentioned that for conventional Inconel 625 materials, the Nb-rich intermetallic phase disappeared for temperatures above 1100 °C, while NbCrO_4 was detected in the corrosion products. He also reported [17] that the resulting chromia scale had a poor adherence. In the present study, the adherence of the oxide scale was quite high for the CM materials but was rather poor for the LBM materials. The evaluation of the cyclic oxidation behaviour of these compounds was outside the scope of the present paper, but the observation of large cracks between $\text{Nb}_{1.5}\text{Cr}_{0.5}\text{O}_4$ and substrate was in agreement with Rolland observations [17]. In fact, the amount of this oxide was high for the LBM alloy in comparison to the amount observed on the cross-section of the CM alloy (Fig. 10). It may be suggested that the homogeneous distribution of this oxide is related to the observed cellular microstructure. Indeed, the high level of Nb segregation in the LBM material, associated with a fine nanometric size microstructure should contribute to the availability of niobium, whereas for the CM material, discontinuous interoxidic NbCrO_4 was present at the interface. In addition, the higher oxidation kinetics of the LBM samples must be taken into account in the discussion of this mechanism. Indeed, because the corrosion rate is higher for the LBM material, the chromium flux and relative depletion in the substrate were also higher. Previous studies [18] nicely confirmed that this Nb-rich oxide forms because the $\delta\text{-Ni}_3\text{Nb}$ layer becomes thermodynamically unstable if the oxygen partial pressure at the chromia-alloy interface increases due to enhanced Cr depletion as a result of an increase in scale growth rate. This increase of chromium depletion led in parallel to an increase in the niobium flux, as proposed by Chyrkin et al. [30], and a higher alloy recession, thus leading to strong Nb enrichment in the subsurface region. Thus, both microstructural and kinetics aspects can explain the continuous nature

of the $\text{Nb}_{1.5}\text{Cr}_{0.5}\text{O}_4$ oxide layer in the case of the LBM sample oxidized at 1050 °C.

The presence of a high density of voids in the alloy subsurface at 1050 °C also indicated that chromium removal was not compensated (Kirkendall effect) by the back diffusion of other elements similar to the CM material for which no voids were observed. It is well known that the transfer of atoms from the alloy to the oxide lattice may involve the generation of a counterflow of vacancies into the substrate (vacancy injection) [32]. The formation of the high density of voids during oxidation was studied by Oquab et al. [33] on a chromia-forming alloy (Fe-25Cr-35Ni-1Nb in wt. %). They showed that the voids were not located at the oxide-alloy interface but, rather, in the sub-surface region, as observed in the present study. They concluded that voids were a result of vacancy condensation at the surface of the internal alumina that acts as the nucleation site. In the present study, the LBM materials were less susceptible to internal oxidation compared to the CM materials but the oxidation rate of CM materials was clearly higher. Consequently, the origin of the voids for LBM material should be mainly attributed to the higher transfer of Cr atoms from alloy to oxide lattice resulting in a high counterflow of vacancies.

Finally, it has to be mentioned that there are differences between the internal oxidation of the CM and LBM materials. The internal oxidation involved mainly grain boundaries in the case of CM materials while the amount of internal oxides was low for the LBM material. Both Jia et al. [14] and Sanviemvongsak et al. [12] observed the formation of TiO_2 and Al_2O_3 intergranular precipitates after exposure at 850 °C of LBM Inconel 718 in air for 100 and 1000 h, respectively. The depth of this intergranular oxidation was related to the volume energy density as reported by Jia et al. [14], and ranged from 15 to 70 μm as the energy density decreases. The depth was much lower in Sanviemvongsak's work, which reported a depth of 2.5 μm after 48 h and 11 μm after 1000 h of oxidation at 850 °C. Consequently, our observation should probably be attributed to the removal of a part of Al, Mn and Ti during powder atomization or laser beam manufacturing, as supported by the EPMA results. Another consequence of the Mn removal was the absence of the $(\text{MnCr})_3\text{O}_4$ spinel layer on top of the chromia scale for LBM materials.

Conclusions

The laser beam melting (LBM) additive manufacturing process was used to produce a plate of the chromia-forming Ni-based superalloy Inconel 625. Its microstructure and air oxidation resistance was studied at 900 °C and 1050 °C. The experimental results were compared to those obtained with a conventionally manufactured (CM) material. The main conclusions can be summarized as follows:

- (1) The obtained LBM microstructures were textured, dendritic and cellular. The formation of the cells resulted in severe Nb and Mo segregation in the interdendritic regions during fast cooling (estimated to $2 \times 10^6 \text{ }^\circ\text{C.s}^{-1}$ from microstructural features).
- (2) The oxidation resistance of the CM material was systematically higher than that of LBM independently of the surface state (as received and ground) and taking into account the real surface area due to roughness imparted by the LBM process. The difference was particularly significant at 1050 °C, whereas the oxidation rate was very close for CM and LBM at 900 °C.
- (3) At 1050 °C, the severe oxidation attack of the LBM material induced the formation of a poorly adherent oxide, a high number of voids in the subsurface region and a large amount of $\text{Nb}_{1.5}\text{Cr}_{0.5}\text{O}_4$ at the oxide-alloy interface. These observations were attributed to the Nb distribution in the LBM samples.
- (4) Internal oxidation was significantly lower for the LBM samples at both temperatures, because of a lower amount of Al in the LBM samples than in the CM samples.

Data availability

The raw/processed data required to reproduce these findings cannot be shared at this time due to time limitations. Raw data of the present study will be made available on demand.

Declaration of Competing Interest

The authors declare that they have no known competing financial interests or personal relationships that could have appeared to influence the work reported in this paper.

Acknowledgements

We are pleased to acknowledge Ms. C. Gendarme, S. Migot, F. Lebel and Dr. J. Ghanbaja for their assistance, respectively, with the EPMA, FIB lamella extraction, confocal characterization and TEM STEM observations. This work was supported by a grant overseen by BPI France in the framework of the F.A.I.R. project.

References

- [1] C.T. Sims, A history of superalloy metallurgy for superalloy metallurgists, *Superalloys 1984* (1984) 399–419.
- [2] H.C. Pai, M. Sundararaman, A comparison of the precipitation kinetics of γ'' particles in virgin and re-solutioned Alloy 625, *Proceedings of the International Symposium on Superalloys Vol. 718* (2005) 625–706.
- [3] D. Gu, *Laser Additive Manufacturing of High-performance Materials*, Springer, 2015.
- [4] D. Herzog, V. Seyda, E. Wycisk, C. Emmelmann, Additive manufacturing of metals, *Acta Mater.* 117 (2016) 371–392.
- [5] L.E. Murr, S.M. Gaytan, D.A. Ramirez, E. Martinez, J. Hernandez, K.N. Amato, R.B. Wicker, Metal fabrication by additive manufacturing using laser and electron beam melting technologies, *J. Mater. Sci. Technol.* 28 (2012) 1–14.
- [6] A. Mostafaie, E.L. Stevens, E.T. Hughes, S.D. Biery, C. Hillia, M. Chmielus, Powder bed binder jet printed alloy 625: densification, microstructure and mechanical properties, *Mater. Des.* 108 (2016) 126–135.
- [7] C.P. Paul, P. Ganesh, S.K. Mishra, P. Bhargava, J.A. Negi, A.K. Nath, Investigating laser rapid manufacturing for Inconel-625 components, *Opt. Laser Technol.* 39 (2007) 800–805.
- [8] P. Ganesh, K. Kaul, C.P. Paul, P. Tiwari, S.K. Rai, R.C. Prasad, L.M. Kukreja, Fatigue and fracture toughness characteristics of laser rapid manufactured Inconel 625 structures, *Mater. Sci. Eng., A* 527 (2010) 7490–7497.
- [9] K. Mumtaz, N. Hopkinson, Selective laser melting of Inconel 625 using pulse shaping, *Rapid Prototyp. J.* 16 (2010) 248–257.
- [10] P.L. Blackwell, The mechanical and microstructural characteristics of laser-deposited IN718, *J. Mater. Process. Technol.* 170 (2005) 240–246.
- [11] X. Zhao, J. Chen, X. Lin, W. Huang, Study on microstructure and mechanical properties of laser rapid forming Inconel 718, *Mater. Sci. Eng., A* 478 (2008) 119–124.
- [12] T. Sanvienwongsak, D. Monceau, B. Macquaire, High temperature oxidation of IN 718 manufactured by laser beam melting and electron beam melting: effect of surface topography, *Corros. Sci.* 141 (2018) 127–145.
- [13] H. Hindam, D.P. Whittle, Microstructure, adhesion and growth kinetics of protective scales on metals and alloys, *Oxid. Met.* 18 (5–6) (1982) 245–284.
- [14] Q. Jia, D. Gu, Selective laser melting additive manufactured Inconel 718 superalloy parts: high-temperature oxidation property and its mechanisms, *Opt. Laser Technol.* 62 (2014) 161–171.
- [15] L. Kumar, R. Venkataramani, M. Sundararaman, P. Mukhopadhyay, S.P. Garg, Studies on the oxidation behavior of Inconel 625 between 873 and 1523 K, *Oxid. Met.* 45 (1996) 221–244.
- [16] K. Staszewska, M. Scendo, Mechanism and kinetics oxidation of Inconel 617 and 625 alloys, *Technical Issues* (2016) 82–89.
- [17] R. Rolland, *Study of the Influence of the Steam Water on High Temperature Oxidation of Chromia Forming Nickel Based Superalloy*, PhD Thesis, Université Blaise Pascal de Clermont-Ferrand, 2012.
- [18] P. Huczkowski, W. Lehnert, H.-H. Angermann, A. Chyrkin, R. Pillai, D. Grüner, E. Hejrani, W.J. Quadakkers, Effect of gas flow rate on oxidation behaviour of alloy 625 in wet air in the temperature range 900–1000 °C, *Mater. Corros.* 68 (2) (2017) 159–170.
- [19] C. Hong, D. Gu, D. Dai, S. Cao, M. Alkhayat, Q. Jia, R. Poprawe, High-temperature oxidation performance and its mechanism of TiC/Inconel 625 composites prepared by laser metal deposition additive manufacturing, *J. Laser Appl.* 27 (2015) S17005.
- [20] D. Monceau, B. Pieraggi, Determination of parabolic rate constants from a local analysis of mass-gain curves, *Oxid. Met.* 50 (1998) 477–493.
- [21] Y.L. Hu, X. Lin, S.Y. Zhang, Y.M. Jiang, X.F. Lu, H.O. Yang, W.D. Huang, Effect of solution heat treatment on the microstructure and mechanical properties of Inconel 625 superalloy fabricated by laser solid forming, *J. Alloys. Compd.* 767 (2018) 330–344.
- [22] I. Yadroitsev, L. Thivillon, P. Bertrand, I. Smurov, Strategy of manufacturing components with designed internal structure by selective laser melting of metallic powder, *App. Surf. Sci.* 254 (2007) 980–983.
- [23] S. Li, Q. Wei, Y. Shi, Z. Zhu, D. Zhang, Microstructure characteristics of Inconel 625 superalloy manufactured by selective laser melting, *J. Mater. Process. Technol.* 31 (2015) 946–952.
- [24] J.H. Yi, J.W. Kang, T.J. Wang, X. Wang, Y.Y. Hu, T. Feng, P.Y. Wu, Effect of laser energy density on the microstructure, mechanical properties, and deformation of Inconel 718 samples fabricated by selective laser melting, *J. Alloys. Compd.* 786 (2019) 481–488.
- [25] S. Ghosh, L. Ma, N. Ofori-Opoku, J.E. Guyer, On the primary spacing and micro-segregation of cellular dendrites in laser deposited Ni–Nb alloys, *Modelling Simul. Mater. Sci. Eng.* 25 (2017) 065002.
- [26] T. Antonsson, H. Fredriksson, The effect of cooling rate on the solidification of INCONEL 718, *Metall. Trans.* 36 (2005) 85–96.
- [27] H. Xiao, S.M. Li, W.J. Xiao, Y.Q. Li, L.M. Cha, J. Mazumder, L.J. Song, Effects of laser modes on Nb segregation and laves phase formation during laser additive manufacturing of nickel-based superalloy, *Mater. Lett.* 188 (2017) 260–262.
- [28] D.J. Young, *High Temperature Oxidation and Corrosion of Metals*, Elsevier, Amsterdam, 2008.
- [29] M. Lenglet, R. Guillamet, J. Lopitaux, B. Hannoyer, Initial stages of oxidation of inconel 718 by FTIR spectroscopy, *Mater. Res. Bull.* 25 (1990) 715–722.
- [30] A. Chyrkin, P. Huczowski, V. Shemet, L. Singheiser, W.J. Quadakkers, Sub-scale depletion and enrichment processes during high temperature oxidation of the nickel base alloy 625 in the temperature range 900–1000 °C, *Oxid. Met.* 75 (2011) 143–166.
- [31] Y. Du, S. Liu, Y.A. Chang, Y. Yang, A thermodynamic modeling of the Cr–Nb–Ni system, *Calphad.* 29 (2005) 140–148.
- [32] C. Desgranges, F. Lequien, E. Aublant, M. Nastar, D. Monceau, Depletion and voids formation in the substrate during high temperature oxidation of Ni–Cr alloys, *Oxid. Met.* 79 (2013) 93–105.
- [33] D. Oquab, N. Xu, D. Monceau, D.J. Young, Subsurface microstructural changes in a cast heat resisting alloy caused by high temperature corrosion, *Corros. Sci.* 52 (2010) 255–262.